Experimental Investigation of the $6s^2\ {}^1S_0 \rightarrow 6s5d\ {}^3D_1$ Magnetic Dipole Transition in Atomic Ytterbium

By Jason E. Stalnaker

Advisor: Professor Dmitry Budker

An undergraduate thesis submitted to the

Department of Physics

at the

UNIVERSITY of CALIFORNIA at BERKELEY

1998

Abstract

We present the results of an ongoing investigation designed to measure the forbidden magnetic dipole transition amplitude for the $6s^2\ {}^1S_0 \rightarrow 6s5d\ {}^3D_1$ transition (408 nm) in atomic ytterbium. The transition is excited in an effusive atiomic beam with a C.W. laser in the presence of crossed D.C. electric and magnetic fields. The fields are arranged to provide interference between the magnetic dipole transition and a Stark-induced transition caused by the electric field. This interference term is separated from the larger Stark-induced transition by switching the direction of the electric field. The transition is observed through fluorescence in the $6s6p\ {}^3P_1 \rightarrow 6s^2\ {}^1S_0$ decay channel at 556 nm. Preliminary measurements allow us to place an upper limit on the $6s^2\ {}^1S_0 \rightarrow 6s5d\ {}^3D_1$ magnetic dipole amplitude of $M1 < 3 \times 10^{-3}\ \mu_B$.

Acknowledgments

I would like to thank Professor Dmitry Budker and Dr. Chris Bowers for all of their patience, advice, and assistance during the past two years and Professor Struart Freedman for all of his support.

Contents

List of Figures

List of Tables

Chapter 1

Introduction

1.1 Atomic Parity Nonconservation

Within an atom the dominant interactions determining the atomic structure are the electromagnetic interactions between the nucleus and the surrounding electrons. These interactions, like all electromagnetic interactions, conserve parity. That is to say, the interactions are unchanged under mirror reflection. The concept of parity can be described quantum mechanically by introducing a parity operator, Π, defined by the relation

$$\langle \overrightarrow{r} | \Pi | \psi \rangle = \langle - \overrightarrow{r} | \psi \rangle \tag{1.1}$$

where $|\psi\rangle$ describes the wave function of some system and $|\overrightarrow{r}\rangle$ denotes the position basis vectors. Physically this corresponds to a mirror reflection of space, followed by a rotation of 180° about an axis perpendicular to the plane of reflection. To say that the electromagnetic interaction conserves parity means the Hamiltonian describing the interaction commutes with the parity operator. Thus, there exists a basis of vectors in state space

which are eigenstates of both the Hamiltonian and the parity operator. Therefore, given the appropriate basis, one can classify the energy eigenstates according to the eigenvalues of the parity operator. Because Π^2 returns the wave function to its initial state, the parity operator has only two possible eigenvalues, ± 1. A state $|\varphi\rangle$ is classified as odd if $\Pi|\varphi\rangle = -|\varphi\rangle$ and even if $\Pi|\varphi\rangle = +|\varphi\rangle$ [1].

The overwhelming dominance of the electromagnetic interaction in the Hamiltonian governing the atomic structure allows the classification of atomic states according to their parity. However, this classification is only approximate due to the presence of another, much smaller, interaction between the nucleus and the surrounding electrons due to the weak force. In the Standard Model this interaction occurs via the exchange of virtual Z^0 bosons between the nucleus and the electrons. This interaction does not conserve parity. Consequently, as a whole, the atomic Hamiltonian does not conserve parity.

Because of the short range of the weak force, this interaction can be well approximated as a point interaction. It is shown in reference [2] that in the limit of an infinitely heavy Z^0 boson and in the nonrelativistic limit, the parity violating part of the potential has the form

$$V_{p.v.} = \frac{G_F}{4\sqrt{2}m_e}\left[\overrightarrow{\sigma}\cdot\overrightarrow{p}\,\delta^3\left(\overrightarrow{r}\right) + \delta^3\left(\overrightarrow{r}\right)\overrightarrow{\sigma}\cdot\overrightarrow{p}\right]Q_W + terms \quad involving \quad nuclear \quad spin, \tag{1.2}$$

where $\overrightarrow{\sigma}$, $\overrightarrow{p}$, are the spin and momentum operators, m_e is the mass of the electron, G_F is the Fermi coupling constant, $\delta^3\left(\overrightarrow{r}\right)$ is the three-dimensional Dirac delta function, and Q_W is the weak charge. The weak charge plays a role in weak interactions analogous to the role played by the electric charge in electromagnetic interactions and can be expressed

as

$$Q_W = -\left[\left(4\sin^2\theta_W - 1\right)Z + N\right], \tag{1.3}$$

where Z is the atomic number, N is the number of neutrons in the nucleus, and θ_W is the weak-mixing angle [2]. The parity-violating property of the potential arises from the $\overrightarrow{\sigma}\cdot\overrightarrow{p}$ term. Since $\overrightarrow{\sigma}$ does not change sign under parity while $\overrightarrow{p}$ does, $\overrightarrow{\sigma}\cdot\overrightarrow{p}$ forms an invariant that it is odd under parity. This means the reflection of space changes the interaction. This unique parity nonconserving feature allows this interaction to be separated from the electromagnetic interaction, allowing the study of neutral weak currents using atoms.

Because of the small size of this interaction, its addition to the atomic Hamiltonian can be accurately treated using perturbation theory. Since the interaction does not conserve parity, the eigenstates of the perturbed Hamiltonian cannot be strictly classified as even or odd. That is to say, the interaction mixes atomic states (as determined by the electromagnetic interaction) of opposite parity. This mixing leads to a slight modification of the optical properties of the atom. In particular, the parity-selection rule for electric dipole, $E1$, transitions, which states that $E1$ transitions can only occur between states of opposite parity, is no longer strictly obeyed. Thus, a small $E1$ transition amplitude can be present between two atomic states with the same nominal parity. As a consequence of the energy denominator which arises in first order perturbation theory, states of opposite parity which are close in energy will have the strongest mixing.

The magnitude of the parity-nonconserving effect is extremely small and it cannot be observed directly. However, the parity-nonconserving amplitude can be observed through interference with a larger, parity-conserving amplitude. One way to do this is

to apply a static electric field to the atoms, which Stark-mixes the atomic states. The perturbation Hamiltonian for a static electric field can be expressed as

$$H_{Stark} = -\overrightarrow{D} \cdot \overrightarrow{E} \tag{1.4}$$

Where $\overrightarrow{D}$ is the electric dipole operator and $\overrightarrow{E}$ is the static electric field. Using first order perturbation theory the eigenstates of the perturbed Hamiltonian, $\left|\varphi_n^1\right\rangle$, become

$$\left|\varphi_n^1\right\rangle = \left|\varphi_n^0\right\rangle - \overrightarrow{E} \cdot \sum_{i,\ m} \frac{\left\langle \varphi_m^0 \left| \overrightarrow{D} \right| \varphi_n^0 \right\rangle}{E_n - E_m} \left|\varphi_m^0\right\rangle . \tag{1.5}$$

where the sum runs over all of the eigenstates of the unperturbed Hamiltonian $\left|\varphi_m^0\right\rangle$. It is important to note that this perturbation is odd under parity. This means that the Hamiltonian due to the electric field only couples opposite parity states. Consequently, if $|\varphi\rangle$ and $|\psi\rangle$ are eigenstates of parity with the same eigenvalue,

$$\langle \psi \left| H_{Stark} \right| \varphi \rangle = 0 \tag{1.6}$$

Thus the sum over the energy eigenstates, $\left|\varphi_m^0\right\rangle$, in equation 1.5 contains only states with parity opposite to that of the unperturbed state of interest.

Because it mixes states of opposite parity, a static electric field can induce an $E1$ amplitude between states which have the same parity in the absence of an electric field. This amplitude, known as a Stark-induced amplitude, is proportional to the magnitude of the electric field. Consequently, the corresponding transition probability is proportional to the square of the electric field. With proper geometry, the $E1$ amplitude due to parity nonconservation can be combined with the Stark-induced amplitude so that the transition rate contains an interference term. This interference term is proportional to both the parity nonconservation amplitude and the Stark-induced amplitude, and is therefore linear

in the electric field. Although the contribution from the interference term is smaller than the contribution from the pure Stark-induced component by a factor of $\frac{2E1_{PNC}}{E1_{Stark}}$, the sign of the interference term changes with a reversal of the electric field while the pure Stark-induced component does not. Thus, changing the direction of the electric field creates an observable asymmetry in the transition probability. This allows for the separation of the component of the transition probability resulting from the interference between the Stark-induced amplitude and the parity nonconserving amplitude.

1.2 Parity Nonconservation in Ytterbium

Atomic parity nonconservation has been successfully observed in many atoms (see reference [3] for a general review). Recently, the high-precision results in thallium [4] and cesium [5] have demonstrated that atomic parity nonconservation experiments provide a unique test of the electroweak theory within the Standard Model. Indeed, the precision of these experiments, ~1% and ~0.3% respectively, has exceeded the theoretical knowledge of the atomic wave functions and the interpretation of the results of these experiments is currently limited by theory.

In [6] a parity nonconservation experiment using the $4f^{14}6s^2\ {}^1S_0 \rightarrow 4f^{14}6s5d\ {}^3D_1$ transition in ytterbium was suggested (see figure 1.1). The transition is a highly forbidden transition between two states of even parity. The effect of the parity-nonconserving interaction is to mix states of odd parity with the $4f^{14}6s5d\ {}^3D_1$ state (see equation 1.2) . The mixing is dominated by the $4f^{14}6s6p\ {}^1P_1$ state because of the small energy difference between it and the ${}^3D_1$ state, 589 cm^{-1}, and the configurations present in the ${}^1P$ state.

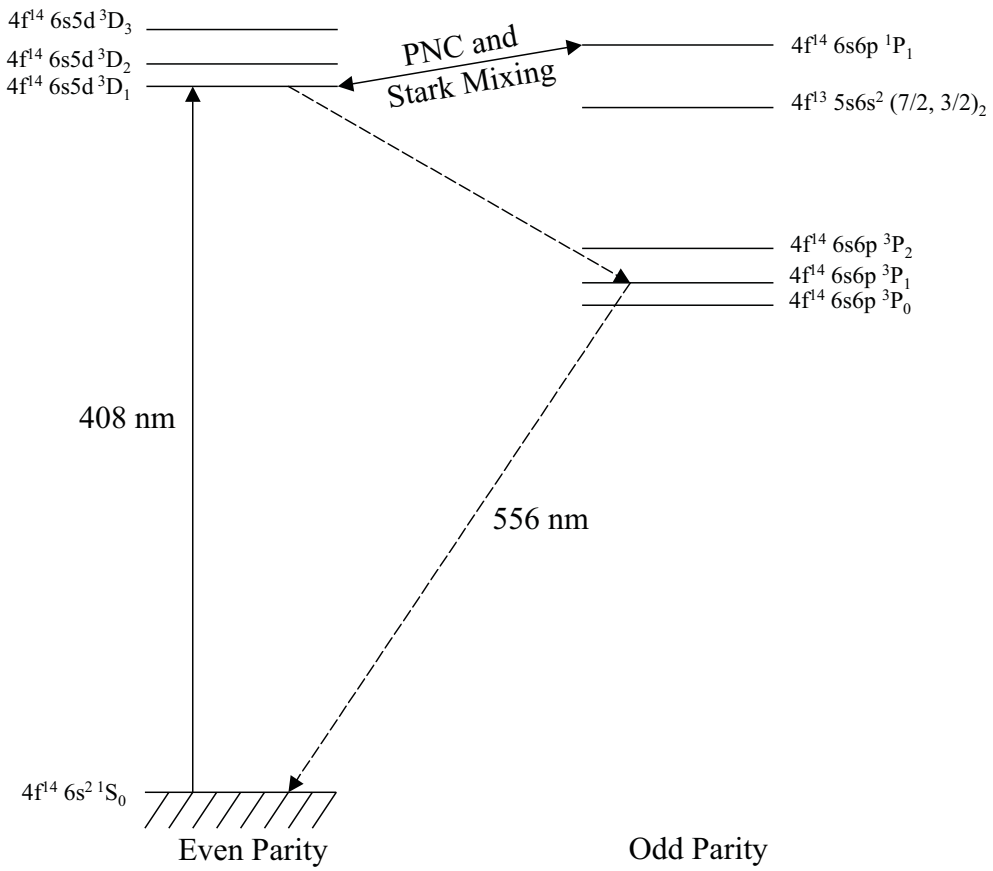

Figure 1.1: Low-lying energy levels in ytterbium.

The enhancement resulting from the small energy difference leads to an estimate of a parity nonconserving amplitude that is ~100 times larger than the amplitude previously studied in Stark-interference experiments in cesium and ~10 times larger than that in thallium [6]. Another important advantage of ytterbium stems from the fact that ytterbium has seven stable isotopes, (^{176}Yb, 12.73% natural abundance; ^{174}Yb, 31.84%; ^{173}Yb, $I = \frac{5}{2}$,16.08%; ^{172}Yb, 21.82%; ^{171}Yb, $I = \frac{1}{2}$,14.27%; ^{170}Yb, 3.03%; ^{168}Yb, 0.135%). Since the value of the weak charge depends upon the number of neutrons in the nucleus (equation 1.3), the parity nonconserving amplitudes are different for the different isotopes. Comparing the parity nonconserving effect for different isotopes would remove the dependence upon knowledge of the atomic wave functions [7]. Thus, a parity nonconservation experiment in ytterbium provides an opportunity to improve the interpretation of atomic parity nonconservation without improving theoretical knowledge of the atomic wave functions. The possibility of performing a parity nonconservation experiment it ytterbium has motivated detailed theoretical and experimental study of the $4f^{14}6s^2\ ^1S_0 \rightarrow 4f^{14}6s5d\ \ ^3D_1$ transition [8] [9] [10].

1.3 M1 Amplitude

Although an $E1$ transition is forbidden because of parity (ignoring the small parity nonconserving amplitude), parity does not forbid a magnetic dipole, $M1$, transition. The presence of a strong $M1$ amplitude, coupled with apparatus imperfections, could mimic the parity-nonconserving amplitude and lead to significant systematic effects in a parity nonconservation experiment using the method of Stark interference. It is therefore important

to know the size of the $M1$ amplitude, or at least to have a sufficiently stringent upper limit, in order to evaluate its effect on a parity nonconservation experiment of the kind proposed in [6]. The current effort to measure the $M1$ amplitude of the $6s^2\ {}^1S_0 \rightarrow 6s5d\ \ {}^3D_1$ transition is the subject of this thesis.

Chapter 2

Properties of the

$6s^2\ {}^1S_0 \rightarrow 6s5d\ \ {}^3D_1$ Transition

2.1 Energy Shifts for the $6s^2\ {}^1S_0 \rightarrow 6s5d\ \ {}^3D_1$ Transition

2.1.1 Isotope Shifts and Hyperfine Structure

The differences in the masses and volumes of the seven different isotopes of ytterbium lead to slight changes in the energies of the atomic states. In addition, the presence of nonzero nuclear spin in the isotopes with an odd number of nucleons leads to energy shifts due to the hyperfine interaction between the electrons and the nucleus. Consequently, a given atomic transition will occur at slightly different frequencies for each of the different isotopic and hyperfine components. The isotope shifts and hyperfine structure of the ${}^1S_0 \rightarrow {}^3D_1$ transition was studied in this laboratory last year [10]. This measurement was done by exciting the ${}^1S_0 \rightarrow {}^3D_1$ transition in an effusive atomic beam in the presence of a

Isotope	**Relative Shift in MHz**
170	2551.3(20)
171	2039.9(14)
172	1110.1(20)
173	624.0(20)
174	0
176	-1060.9(20)
	Hyperfine Structure Constants
171(I=1/2)	$A = -2042.2(19)$
173(I=5/2)	$A = 562.8(5)$ $B = 337.2(19)$

Table 2.1: Experimental values for the isotope shifts and hyperfine structure constants for the $6s^2\ ^1S_0 \rightarrow 4f^{14}6s5d\ \ ^3D_1$ transition

static electric field with a frequency scannable CW laser at 408 nm. The transition was detected through fluorescence from the second stage in the cascade decay of the $6s5d\ \ ^3D_1 \rightarrow 6s5d\ \ ^3P_1 \rightarrow 6s^2\ \ ^1S_0$ transition at 556 nm (figure 1.1). The results of this measurement are summarized in table 2.1, where the energy shifts of the hyperfine structure are given in terms of the hyperfine structure constants A and B. The energy shift due to the hyperfine structure can be computed according to

$$\Delta E_{H.F.} = \frac{1}{2}AC + \frac{B}{8(2I-1)J(2J-1)}\left[3C(C+1) - 4I(I+1)J(J+1)\right], \tag{2.1}$$

where

$$C = F(F+1) - J(J+1) - I(I+1), \tag{2.2}$$

and F is the total angular momentum of the atom, I is the angular momentum of the nucleus, and J is the total electronic angular momentum [11]. The isotope shift for ^{168}Yb was not measured because its isotopic abundance was too small for the transition to be observed.

2.1.2 Stark Shifts

In addition to the hyperfine structure and isotope shifts, there is a shift in the energy for the atomic states when a D.C. electric field is applied to the atoms, known as the Stark shift. The relative Stark shifts of the $^1S_0$ and $^3D_1$ states were also measured in this laboratory [10]. The results of this measurement are

$$\alpha_0\left(^3D_1\right) - \alpha_0\left(^1S_0\right) = -21.6(8)\ kHz/(kV/cm)^2$$
$$\alpha_2\left(^3D_1\right) = 7.0(10)\ kHz/(kV/cm)^2, \tag{2.3}$$

where $\alpha_0(^3D_1)$ and $\alpha_0(^1S_0)$ are the scalar Stark polarizabilities of the $^3D_1$ and $^1S_0$ states and $\alpha_2(^3D_1)$ is the tensor Stark polarizability of the $^3D_1$ state. The energy shifts for the M_J magnetic sublevels of the even isotopes, $I = 0$, are given by [12]

$$\Delta E(\gamma J M_J) = -\frac{1}{2}\left(\alpha_0(\gamma J) + \alpha_2(\gamma J)\frac{3M_J^2 - J(J+1)}{J(2J-1)}\right), \tag{2.4}$$

where J is the electronic angular momentum of the state and γ represents all other quantum numbers required to specify the state. For the odd isotopes the energy shifts for the M_F magnetic sublevels are given by

$$\Delta E(\gamma F M_F) = -\frac{1}{2}\left(\alpha_0(\gamma F) + \alpha_2'(\gamma F)\frac{3M_F^2 - F(F+1)}{F(2F-1)}\right), \tag{2.5}$$

where

$$\alpha_0(\gamma F) = \alpha_0(\gamma J) \tag{2.6}$$

and

$$\alpha_2'(\gamma F) = (-1)^{(I+J+F)}\sqrt{\frac{F(2F-1)(2F+1)(2J+3)(2J+1)(J+1)}{(2F+3)(F+1)J(2J-1)}} \times \begin{Bmatrix} F & J & I \\ J & F & 2 \end{Bmatrix}\alpha_2(\gamma J), \tag{2.7}$$

and F is the total angular momentum of the atom, J is the electronic angular momentum, I is the nuclear spin, and $\begin{Bmatrix} F & J & I \\ J & F & 2 \end{Bmatrix}$ is the Racah six-J symbol.

2.1.3 Magnetic Field Splitting

In order to measure the $M1$ transition amplitude it is necessary to separate the different magnetic components by applying a static magnetic field (see chapter 2). This also results in shifts of the energy levels due to the Zeeman effect. For the even isotopes the low-field Zeeman splitting is given by

$$\Delta E_{Zeeman}(^3D_1, m = \pm 1) = \pm \frac{g\left(^3D_1\right)}{\hbar} \mu_B \overrightarrow{J} \cdot \overrightarrow{B}, \tag{2.8}$$

where μ_B is the Bohr magneton, $\overrightarrow{J}$ is the electronic angular momentum, and $g\left(^3D_1\right)$ is the g-value of the $^3D_1$ state[1]. The g-value of the $^3D_1$ state is [13]

$$g\left(^3D_1\right) = 0.50. \tag{2.9}$$

For the odd-isotopes the hyperfine splitting is larger than the Zeeman shift required to resolve the magnetic sublevels. However, because the hyperfine splitting is not overwhelmingly dominant, a numerical calculation was performed in which the effects of the hyperfine splitting and the applied magnetic field were added simultaneously as a single perturbation to the atomic Hamiltonian. The results of such a calculation, including the relative intensities is shown in figure 2.1. The relative intensities were calculated assuming a static electric field in the z-direction and light polarized in the x-direction. With this geometry, the $M_J = 0$ sublevel of the even isotopes is not excited and only the $M_J = \pm 1$ sublevels appear in figure 2.1 (see section 2.3). For simplicity, the Stark shifts were not include in

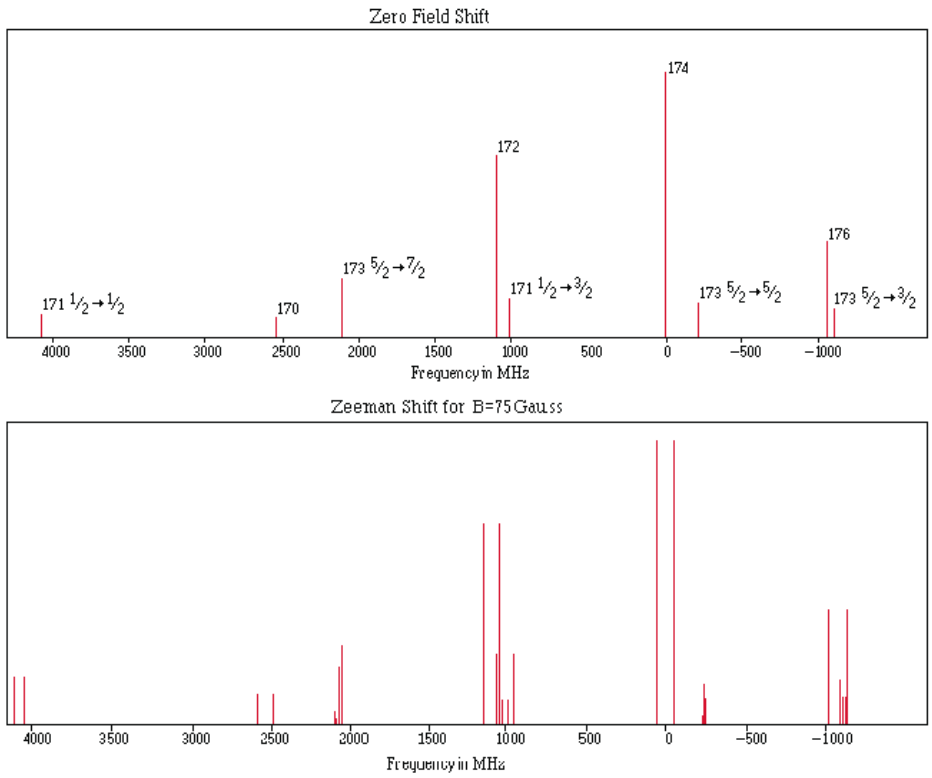

Figure 2.1: Theoretical calculation of the Zeeman splitting for 75 Gauss field and the zero field splitting. The heights indicate the relative intensities.

the calculation. Because the relative Stark shifts between the hyperfine components are typically 20 MHz, its inclusion would not significantly alter the results of the calculation.

2.2 The M1 Transition

Although an $M1$ amplitude for the $6s^2\ ^1S_0 \rightarrow 6s5d\ \ ^3D_1$ transition is not forbidden by parity, it is still highly suppressed due to other selection rules. Indeed, it is forbidden by both radial wave function and angular momentum considerations. $M1$ transitions occur through the coupling of the magnetic dipole moment of an atom with the magnetic field of

the electromagnetic wave. Thus, the Hamiltonian governing the interaction does not affect the radial wave function of the atom or the total orbital angular momentum and total spin, but can only change the projection of the angular momentum and spin along a chosen axis. Because radial wave functions with different principal quantum numbers are orthogonal within the one-electron approximation, $M1$ transitions are forbidden between states with differing principle quantum numbers [14]. Similarly, wave functions with differing orbital angular momentum or differing spin are also orthogonal, making $M1$ transitions between such states forbidden.

The first of these selection rules breaks down if the one-electron configurations are significantly altered by the presence of the other atomic electrons, resulting in configuration mixing. Because this effect only concerns the electron configurations, it cannot mix states of with different orbital angular momentum and spin [14]. However, the presence of the spin-orbit interaction can mix states with different orbital angular momentum and spin, but cannot mix states with different configurations [15]. Thus, it is necessary to have both configuration mixing and spin-orbit mixing in both the $^1S_0$ and the $^3D_1$states if a nonzero $M1$ amplitude is to exist [6]. By considering the possible states that could lead to a finite transition probability, the $M1$ transition amplitude was estimated in reference [6] to be:

$$M1 \lessapprox 10^{-4}\mu_B, \tag{2.10}$$

where μ_B is the Bohr magneton.

The $M1$ $|\,^1S_0, M=0\rangle \rightarrow |\,^3D_1, M\rangle$ transition amplitude for the even isotopes, all

of which have nuclear spin, I, equal to zero, can be written as

$$\begin{aligned} M1_{M'} &= \overrightarrow{ß} \cdot \left\langle {}^1S_0,\ M=0 \left| \overrightarrow{\mu} \right| \ {}^3D_1,\ M' \right\rangle \\ &= \sum_{q=\pm 1,0} (-1)^q ß_{-q} \left\langle {}^1S_0,\ M=0 \left| \mu_q \right| \ {}^3D_1,\ M' \right\rangle \end{aligned} \tag{2.11}$$

where $\overrightarrow{ß}$ is the magnetic field of the light, $\overrightarrow{\mu}$ is the electronic magnetic moment, $ß_q$ and μ_q are the projections of the electric field and magnetic moment along the spherical basis vectors

$$\begin{aligned} \widehat{e}_{-1} &= \frac{1}{\sqrt{2}} \left(\widehat{x} - i\, \widehat{y} \right) \\ \widehat{e}_0 &= \widehat{z} \\ \widehat{e}_{+1} &= -\frac{1}{\sqrt{2}} \left(\widehat{x} + i\, \widehat{y} \right), \end{aligned} \tag{2.12}$$

and M and M' are the projections of the total angular momentum J, J', of the ${}^1S_0$ and ${}^3D_1$ states along the z-axis. Applying the Wigner-Eckhart theorem to equation 2.11 gives [14]

$$M1_{M'} = \sum_{q=\pm 1,0} (-1)^q \begin{pmatrix} 0 & 1 & 1 \\ 0 & q & M' \end{pmatrix} ß_{-q} \left({}^1S_0 \left\| \mu \right\| \ {}^3D_1 \right), \tag{2.13}$$

where $\left({}^1S_0 \left\| \mu \right\| \ {}^3D_1 \right)$ is the reduced matrix element and $\begin{pmatrix} 0 & 1 & 1 \\ 0 & q & M' \end{pmatrix}$ is the Racah three-J symbol. Using equation 2.12 to rewrite equation 2.13 in the more familiar Cartesian coordinates and evaluating the three-J symbols gives

$$\begin{aligned} M1_{M'} = & \tfrac{1}{\sqrt{6}} \left[ß_x + i\, ß_y \right] \left({}^1S_0 \left\| \mu \right\| \ {}^3D_1 \right) \delta_{M',-1} \\ & - \tfrac{1}{\sqrt{6}} \left[ß_x - i\, ß_y \right] \left({}^1S_0 \left\| \mu \right\| \ {}^3D_1 \right) \delta_{M',+1} \\ & - \tfrac{1}{\sqrt{3}} ß_z \left({}^1S_0 \left\| \mu \right\| \ {}^3D_1 \right) \delta_{M',0} \end{aligned} \tag{2.14}$$

where $ß_i$ is the projection of the vectors $\overrightarrow{ß}$ along the Cartesian basis vectors and $\delta_{M',q}$ is the Kronecker Delta.

The transition amplitudes for isotopes with nonzero nuclear spin, I, between states with total angular momentum, F and F', can be related to the reduced matrix element above according to [14]

$$\left({}^1S_0,\ I,\ F\left\|\mu\right\|{}^3D_1,\ I,\ F'\right) = (-1)^{I+F'+1}\left({}^1S_0\left\|\mu\right\|{}^3D_1\right)\times \sqrt{(2F+1)\,(2F'+1)}\begin{Bmatrix} 0 & F & I \\ F' & I' & 1 \end{Bmatrix}. \tag{2.15}$$

The Wigner-Eckhart theorem can then be used to find the transition amplitude between states with specific projections of the total angular momentum along the z-axis. The results of such a calculation for the hyperfine components of the two odd isotopes are

$$\begin{aligned}
\text{For } {}^{171}\text{Yb}: &\left({}^1S_0, I=\frac{1}{2},\ F=\frac{1}{2}\left\|\mu\right\|{}^3D_1,\ I=\frac{1}{2}\ ,\ F'=\frac{1}{2}\right) = 0.816\left({}^1S_0\left\|\mu\right\|{}^3D_1\right)\\
\text{For } {}^{173}\text{Yb}: &\left({}^1S_0,\ I=\frac{5}{2},\ F=\frac{5}{2}\left\|\mu\right\|{}^3D_1,\ I=\frac{5}{2},\ F'=\frac{3}{2}\right) = 1.155\left({}^1S_0\left\|\mu\right\|{}^3D_1\right)\\
: &\left({}^1S_0,\ I=\frac{5}{2},\ F=\frac{5}{2}\left\|\mu\right\|{}^3D_1,\ I=\frac{5}{2},\ F'=\frac{5}{2}\right) = 1.414\left({}^1S_0\left\|\mu\right\|{}^3D_1\right)\\
: &\left({}^1S_0,\ I=\frac{5}{2},\ F=\frac{5}{2}\left\|\mu\right\|{}^3D_1,\ I=\frac{5}{2},\ F'=\frac{7}{2}\right) = 1.633\left({}^1S_0\left\|\mu\right\|{}^3D_1\right)
\end{aligned} \tag{2.16}$$

Thus, a measurement of the $M1$ amplitude in one of the even isotopes allows calculation of the $M1$ amplitude in all of the other isotopes and hyperfine components.

2.3 The Stark-Induced Transition

The $M1$ amplitude as estimated in [6] is too small to be observed directly. This difficulty can be overcome by interfering the small $M1$ amplitude with a larger amplitude created by a static electric field in a manner similar to the method described in the introduction for interfering the parity nonconservation amplitude.

Because of the closeness in the energy of the $6s5d\ ^3D_1$ and $6s6p\ ^1P_1$ states the sum in equation 1.5 is dominated by the $6s6p\ ^1P_1$ state [6]. To a good approximation equation the perturbed $6s5d\ ^3D_1$ state can be written as

$$\left|\widetilde{^3D_1, M}\right\rangle = \left|^3D_1, M\right\rangle - \sum_M \frac{\left\langle ^1P_1, M' \left| \overrightarrow{D} \cdot \overrightarrow{E} \right| \ ^3D_1, M \right\rangle}{E(^3D_1) - E(^1P_1)} \left|^1P_1\right\rangle, \tag{2.17}$$

where $\left|\widetilde{^3D_1, M}\right\rangle$ is the perturbed $6s5d\ ^3D_1$state, $E(^3D_1)$ and $E(^1P_1)$ are the energies of the $6s5d\ ^3D_1$ and $6s6p\ ^1P_1$ states. Since the mixing of the $^3D_1$ and $^1P_1$ states is large and the $6s^2\ ^1S_0 \rightarrow 6s6p\ ^1P_1$ transition is a strong $E1$ transition, a sizable transition amplitude between the $\left|\ ^1S_0\right\rangle$ and $\left|\widetilde{^3D_1}\right\rangle$ states is induced with experimentally achievable electric fields.

To illustrate the properties of the Stark-induced amplitude we consider the following analysis. We choose a coordinate system with the z-axis directed along the direction of the static electric field. In order to determine the mixing between the different magnetic sublevels of the $^3D_1$ and $^1P_1$ states resulting from the static electric field we apply the Wigner-Eckhart theorem to equation 2.17.

$$\left|\widetilde{^3D_1, M}\right\rangle = \left|^3D_1, M\right\rangle - \sum_{M'=\pm1,0} (-1)^{1-M+M'} \begin{pmatrix} 1 & 1 & 1 \\ -M' & 0 & M \end{pmatrix} \frac{E\ \left(^1P_1 \left\| D \right\| \ ^3D_1\right)}{E(^3D_1) - E(^1P_1)} \left|^1P_1, M'\right\rangle. \tag{2.18}$$

The $E1$ transition amplitude between the $^1S_0$ state and perturbed $^3D_1, M'$ state is therefore given by

$$\left\langle ^1S_0 \left| \overrightarrow{\varepsilon} \cdot \overrightarrow{D} \right| \widetilde{^3D_1, M} \right\rangle = - \sum_{M'=\pm1,0} (-1)^{1-M+M'} \begin{pmatrix} 1 & 1 & 1 \\ -M' & 0 & M \end{pmatrix} \frac{E\ \left(^1P_1 \left\| D \right\| \ ^3D_1\right)}{E(^3D_1) - E(^1P_1)} \times \left\langle ^1S_0 \left| \overrightarrow{\varepsilon} \cdot \overrightarrow{D} \right| \ ^1P_1, M' \right\rangle. \tag{2.19}$$

To see which transitions are allowed we apply the Wigner-Eckhart theorem once again and sum over M' giving

$$\left\langle {}^1S_0 \left| \overrightarrow{\varepsilon} \cdot \overrightarrow{D} \right| \widetilde{{}^3D_1, M} \right\rangle = - \sum_{q=\pm 1,0} (-1)^{1-M} \left| \widehat{\varepsilon}_{-q} \right| \begin{pmatrix} 1 & 1 & 1 \\ q & 0 & M \end{pmatrix} \times \begin{pmatrix} 0 & 1 & 1 \\ 0 & q & M \end{pmatrix} \frac{E \left({}^1P_1 \left\| D \right\| {}^3D_1 \right)}{E({}^3D_1) - E({}^1P_1)} \varepsilon \left({}^1S_0 \left\| D \right\|^1 P_1 \right) \tag{2.20}$$

$$= (-1)^{1-M} \left| \widehat{\varepsilon}_{-M} \right| \begin{pmatrix} 1 & 1 & 1 \\ -M & 0 & M \end{pmatrix} \begin{pmatrix} 0 & 1 & 1 \\ 0 & -M & M \end{pmatrix} \tag{2.21}$$

$$\times \frac{E \left({}^1P_1 \left\| D \right\| {}^3D_1 \right)}{E({}^3D_1) - E({}^1P_1)} \varepsilon \left({}^1S_0 \left\| D \right\|^1 P_1 \right) \tag{2.22}$$

where $\widehat{\varepsilon}_q$ is the projection of the unit vector $\widehat{\varepsilon}$ along the spherical basis vector $\widehat{e}_q$. Because

$$\begin{pmatrix} 1 & 1 & 1 \\ 0 & 0 & 0 \end{pmatrix} = 0 \tag{2.23}$$

equation 2.20 shows that the $\left| \widetilde{{}^3D_1, M = 0} \right\rangle$ cannot be excited if the direction of the electric field is along the z-axis, and that the component of $\overrightarrow{\varepsilon}$ which is parallel to the electric field does not contribute to the transition amplitude. Thus, we can only consider light polarized in the x-y plane and write

$$\widehat{\varepsilon} = a\widehat{x} + b\widehat{y} = a \left(\frac{1}{\sqrt{2}} \left(\widehat{e}_{-1} - \widehat{e}_{+1} \right) \right) + b \left(\frac{-i}{\sqrt{2}} \left(\widehat{e}_{-1} + \widehat{e}_{+1} \right) \right) \tag{2.24}$$

where

$$|a|^2 + |b|^2 = 1. \tag{2.25}$$

Substituting equation 2.24 into equation 2.20 and evaluating it for the case of $M = \pm 1$ gives

$$\left\langle {}^1S_0 \left| \overrightarrow{\varepsilon} \cdot \overrightarrow{D} \right| {}^3D_1, \widetilde{M = \pm 1} \right\rangle = \frac{1}{6}(a \mp ib) \frac{E \left({}^1P_1 \| D \| {}^3D_1 \right)}{E({}^3D_1) - E({}^1P_1)} \left({}^1S_0 \| D \| {}^1P_1 \right). \tag{2.26}$$

Noting that

$$\overrightarrow{E} \times \overrightarrow{\varepsilon} = \left[\frac{1}{\sqrt{2}}(a - ib)\widehat{e}_{-1} - \frac{1}{\sqrt{2}}(a + ib)\widehat{e}_{+1} \right] E, \tag{2.27}$$

we see that it is possible to write the Stark-induced amplitude as

$$\left\langle {}^1S_0 \left| \overrightarrow{\varepsilon} \cdot \overrightarrow{R} \right| {}^3D_1, \widetilde{M = \pm 1} \right\rangle \equiv E1_{Stark} = i\beta \left(\overrightarrow{E} \times \overrightarrow{\varepsilon} \right)_M, \tag{2.28}$$

where $\left(\overrightarrow{E} \times \overrightarrow{\varepsilon} \right)_M$ is the e_M component of the vector $\overrightarrow{E} \times \overrightarrow{\varepsilon}$ and β is a real number [8]. Using this simplified notation we see that for a generalized coordinate system $E1_{Stark}$ becomes

$$E1_{Stark \quad M'} = \begin{array}{c} -\frac{i\beta}{\sqrt{2}} \left[\left(\overrightarrow{E} \times \overrightarrow{\varepsilon} \right)_x + i \left(\overrightarrow{E} \times \overrightarrow{\varepsilon} \right)_y \right] \delta_{M',+1} + \\ \frac{i\beta}{\sqrt{2}} \left[\left(\overrightarrow{E} \times \overrightarrow{\varepsilon} \right)_x - i \left(\overrightarrow{E} \times \overrightarrow{\varepsilon} \right)_y \right] \delta_{M',-1} + i\beta \left(\overrightarrow{E} \times \overrightarrow{\varepsilon} \right)_z \delta_{M',0}. \end{array} \tag{2.29}$$

The magnitude of β was measured to be

$$|\beta| = 2.18(33) \times 10^{-8} \frac{ea_0}{V/cm} \tag{2.30}$$

in this laboratory [10]

2.4 Interference of the Stark-Induced Amplitude and the M1 Amplitude

Interference between two amplitudes is only possible if the amplitudes are either both real or both imaginary and the amplitudes couple to the same quantum states. To

illustrate how this interference occurs, we consider the following experimental setup. A static electric field is applied to a sample of atoms, generating a Stark-induced amplitude. This direction is used to define the y axis of a coordinate system. From equation 2.28, only light polarizations perpendicular to the electric field contribute to the Stark transition amplitude. Thus, the direction of the polarization of the light used to excite the transition is chosen to be perpendicular to the electric field. This direction is used to define the z axis. With this geometry, equation 2.29 shows that the resulting amplitude is purely imaginary. Hence, the direction of the magnetic field of the light, $\overrightarrow{ß}$, must be chosen so that the resulting $M1$ amplitude is also imaginary. From equation 2.2 we see that this occurs when $\widehat{ß} = \widehat{y}$. Noting that $\widehat{ß} = \widehat{k} \times \widehat{\varepsilon}$, where $\widehat{k}$ is the direction of the propagation of the light, we have $\widehat{k} = \widehat{x}$ (see figure 2.2). This geometry gives a transition probability of

$$M1 + E1_{Stark} = \left[\frac{i}{\sqrt{6}} ß \left({}^1S_0 \left\| \mu \right\| {}^3D_1 \right) - \frac{i}{\sqrt{2}} \beta \left(\overrightarrow{E} \times \overrightarrow{\varepsilon} \right)_x \right] \delta_{M,+1} + \left[\frac{i}{\sqrt{6}} ß \left({}^1S_0 \left\| \mu \right\| {}^3D_1 \right) + \frac{i}{\sqrt{2}} \beta \left(\overrightarrow{E} \times \overrightarrow{\varepsilon} \right)_x \right] \delta_{M,-1} \tag{2.31}$$

Although, the $M1$ and the $E1_{Stark}$ contributions to the amplitude are both imaginary, the interference term for the $M = +1$ and the $M = -1$ contributions are of opposite sign. This means that if both of the magnetic sublevels are excited simultaneously, as is the case for y-polarized light, the two interference terms will cancel in the transition probability. One way to circumvent this problem is to apply a static magnetic field, $\overrightarrow{B}$, along the z axis. This causes the energies of the $M = +1$ and $M = -1$ magnetic sublevels shift in opposite directions (see equation 2.8). Given a sufficiently strong magnetic field, it is possible to resolve the energies of the two magnetic sublevels and to excite only one of the magnetic

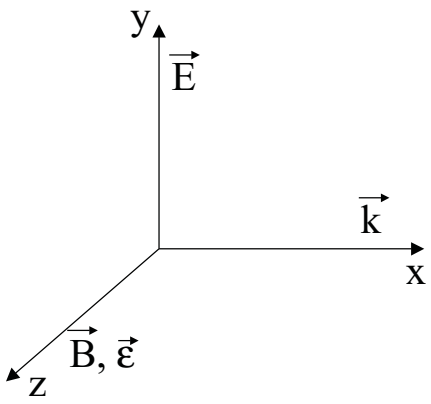

Figure 2.2: Experimental geometry for $M1$ measurement

sublevels with narrow-band light. In this case the transition probability is given by

$$P\left(M1+E1_{Stark}\right)_{M=\pm1} = \left|M1+E1_{Stark}\right|^2 = \left[\begin{array}{c} \frac{1}{6}ß\left({}^1S_0\left\|\mu\right\|{}^3D_1\right)^2 + \\ \frac{1}{2}\beta^2\left(\overrightarrow{E}\times\overrightarrow{\varepsilon}\right)_x^2 \pm \\ \frac{\beta}{3}ß\left({}^1S_0\left\|\mu\right\|{}^3D_1\right)\left(\overrightarrow{E}\times\overrightarrow{\varepsilon}\right)_x \end{array}\right]\delta_{M,\pm1}. \tag{2.32}$$

At electric fields greater than ~10kV/cm, the estimate in equation 2.10 gives an $M1$ transition probability which is $\sim 2\times10^{-6}$ times smaller than the $E1_{Stark}$ transition probability. Thus, the term due solely to the $M1$ amplitude may be discarded. This leaves the terms from the Stark-induced amplitude and the interference term

$$P\left(M1+E1_{Stark}\right)_{M=\pm1} = \left|M1+E1_{Stark}\right|^2 = \left[\begin{array}{c} \frac{1}{2}\beta^2\left(\overrightarrow{E}\times\overrightarrow{\varepsilon}\right)_x^2 \pm \\ \frac{\beta}{3}ß\left({}^1S_0\left\|\mu\right\|{}^3D_1\right)\left(\overrightarrow{E}\times\overrightarrow{\varepsilon}\right)_x \end{array}\right]\delta_{M,\pm1}. \tag{2.33}$$

The contribution due to the Stark-induced amplitude alone is proportional to the square

of the electric field while the interference term is linear in the electric field. This means there will be an asymmetry in the transition probability, equal to the ratio of $\frac{2M1}{\beta E}$,with the reversal of the direction of the electric field. Using the estimate of the $M1$ amplitude given above, along with the measured value of β gives an asymmetry of

$$\frac{0.002}{\text{E / 10 kV/cm}}. \tag{2.34}$$

Although the asymmetry increases with decreasing electric field, the statistical sensitivity increases with the square root of the signal size. Since the signal size is proportional to the square of the electric field, the statistical sensitivity is proportional to the magnitude of the electric field. Thus, if the measurement is limited by statistical noise, there is no advantage to decreasing the electric field.

In addition to reversal of the electric field direction, reversing the direction of the magnetic field also produces a change in the sign of asymmetry since switching the magnetic field changes the magnetic sublevel excited (see equation 2.33). This additional reversal can be used to distinguish the real $M1$-$E1_{Stark}$ interference terms from possible systematic effects.

Chapter 3

Experimental Apparatus

A block diagram of the apparatus used to make a preliminary measurement of the $M1$ amplitude is shown in figure 3.1. An effusive atomic beam of natural ytterbium was excited by light at 408 nm in the presence of crossed D.C. electric and magnetic fields. Fluorescence from the decay of the $6s5d\ ^3P_1 \rightarrow 6s^2\ ^1S_0$ at 556nm was detected with a photomultiplier tube. The current from the photomultiplier tube was sent through a current to voltage converter with a low-pass filter and was detected with an analog to digital converter and stored on a personal computer. The direction of the electric field was switched at ~0.7 Hz by a signal generated from the computer.

Much of the apparatus described here was also used to measure the Stark-induced amplitude and energy shifts of the $6s^2\ ^1S_1 \rightarrow 5d6s\ ^3D_1$ transition. In particular, the light source, atomic beam, vacuum chamber, and electric field plates were used in these previous measurements and were unmodified for this measurement. Consequently, these parts of the apparatus are described in detail in reference [10].

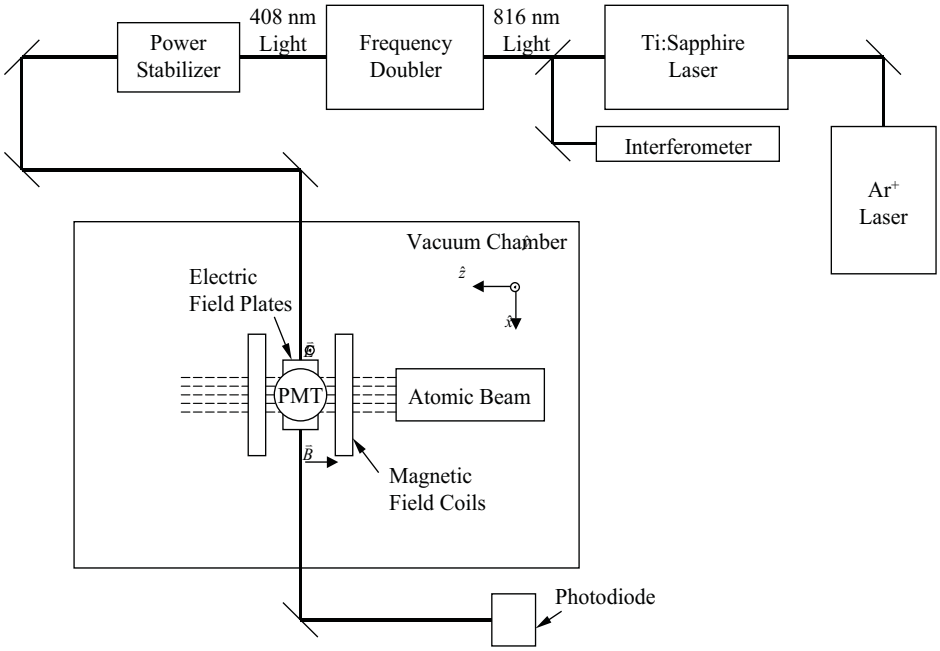

Figure 3.1: A block diagram of apparatus

3.1 Light Source

3.1.1 Laser at 816 nm

Light at 408.344 nm (vacuum wavelength) is required to excite the $6s^2\ ^1S_1 \rightarrow 5d6s\ ^3D_1$ transition. The light was created by frequency doubling light at 816.689 nm from a CW Ti:sapphire laser. This was created using a Titan-CW single-mode ring laser made by Schwarz Electro-Optics which had been modified to make it continuously frequency scannable over a 20 GHz range. These modifications are described in detail in [10]. The Ti:sapphire crystal was pumped with all lines from a Spectra-Physics 2080 Ar^+ laser which was operated at ~8 watts. The Ti:sapphire laser produced ~1 watt of light at 816nm. In order to achieve high frequency stability the Ti:sapphire laser was locked to an external, temperature stabilized, commercial, Fabry-Perot interferometer with a free-spectral-range of 150 MHz (Burleigh CFT-500) using the FM-sideband locking technique [16]. The length of the Fabry-Perot interferometer could be changed by applying a voltage to a PZT mirror mount within the interferometer. By varying the length of the interferometer the frequency of maximum transmission of the light through the interferometer. The laser frequency could therefore be scanned by changing the voltage applied to the PZT, making the laser scannable by a voltage signal generated from the computer.

The 816.689 nm light required from the Ti:sapphire laser is very close to a broad water vapor resonance absorption line at 816.678 nm. The presence of this line introduced sufficient loss in the laser cavity to prevent lasing at 816.689 nm. The absorption due to water vapor was estimated to be ~10^{-3} within the 1 m cavity [10]. This difficulty was overcome by introducing a thin etalon in the cavity to prevent lasing in adjacent transmission

peaks of a thicker etalon inside the cavity. Additionally, it was necessary to create a steady flow of dry nitrogen through the laser cavity when the laser was used [10].

3.1.2 Frequency Doubler

The 816 nm light from the Ti:sapphire laser was sent into a commercial, external frequency doubling unit (Laser Analytical Systems, Wavetrain CW frequency doubler). The doubling unit consisted of an LBO crystal placed at the focus of a ring cavity. The length of the cavity was locked to the Ti:sapphire laser frequency using the Hänsch-Couillaud method [17].

When first setup, the efficiency of the doubling cavity was 8% at 300 mW of pump power. This decreased in time, resulting in only 2% efficiency at 900 mW. This decrease was attributed to degradation of the surface of the crystal due to water vapor. When a new crystal was placed in the cavity the efficiency increased to 16% at 900 mW. Although the new LBO doubling crystal allowed for significantly more power out of the doubler, it also was seen to make the frequency doubling cavity more sensitive to the water vapor absorption line at 816.678 nm. With the old crystal the water vapor absorption line created a minor reduction in the power in the cavity, but the doubler remained locked at the frequency of the $^1S_1 \rightarrow {}^3D_1$ transition. With the new crystal, the doubler was unable to remain locked near the $^1S_1 \rightarrow {}^3D_1$ resonance. A flow of dry nitrogen was setup in an effort to purge the water from the cavity. Although this allowed the laser to maintain the lock closer to the desired frequency, the frequency doubler was still unable to remain locked as the laser scanned across the frequency for the $^1S_1 \rightarrow {}^3D_1$ resonance. Consequently, the old crystal was temporarily put back into the cavity and was used to make the measurements described

here. This problem will be addressed in the near future. The power out of the frequency doubler was ~15 mW for the measurements described here.

3.1.3 Intensity Stabilizer

In order to achieve high stability in laser power the 408 nm light was sent through a commercial laser power stabilizer made by Cambridge Research and Instrumentation (Model LS100). A photodiode detects a small amount of the light which is picked off from a beamsplitter. This is used to create an error signal which controls the voltage applied to a Pockels cell. The Pockels cell in conjunction with an output polarizer acts as a voltage controlled retardation plate causing the transmission through the cell to vary with the voltage applied. The D.C. stabilization was seen to be 1 part in 10^4 over the course of a frequency scan with short term fluctuations around 1 part in 100.

Although the power stabilizer was able to stabilize the signal quite well, it introduced a significant loss in laser power. The power was reduced by approximately one-third its initial value, giving ~5 mW of light for the measurements described here.

3.2 Atomic Beam and Vacuum Chamber

The atomic beam was created inside a vacuum chamber which was evacuated to a residual pressure of ~5×10^{-6} Torr. The vacuum was maintained with a turbo pump with a pumping speed of 170 liters per second and a 120 cm^2 liquid nitrogen trap. The atomic beam was created by resistively heating a 6 in long 2 in diameter stainless steel tube containing ytterbium nuggets. Flanges were attached to the front and rear of the tube.

The front flange consisted of a 0.19 in thick piece of stainless steel in which a continuous zig-zag pattern was cut. The zig-zag pattern was created using wire electric discharge machine with 0.010 in wire. The zig-zag pattern covered an area 0.2 in in the vertical direction and 0.75 in in the horizontal direction. The cuts in the flange gave a transparency of ~50% in the forward direction while reducing the amount of ytterbium leaving the oven at large angles. This prevents the build up of ytterbium inside the chamber and decreases the amount of ytterbium wasted. The oven was heated using thermo-coax cables attached to the tube and the flanges. The front of the oven was kept ~30°C hotter than the rear, as measured with thermocouples, so that ytterbium would not build up in the channels in the front flange. The oven was operated at ~480°C, corresponding to a vapor pressure of ~10^{-2} Torr.

3.3 Electric Field

3.3.1 Electric Field Plates

The electric field plates were made of stainless steel and measured 3.2 cm along the direction of the atomic beam, 8.9 cm in the direction of the laser beam, and 0.79 cm thick. The edges of the plates were rounded to reduce discharges. A depression 2.3 cm along the laser beam, 1.3 cm along the atomic beam, was cut into the top field plate giving it a thickness of 0.12 cm. In this region 198 holes with 0.12 cm diameter were drilled through so that the fluorescence could be detected directly above the electric field plates. The plates were separated by 1.016 cm by two Delrin spacers, positioned perpendicular to the laser beam. Holes 0.5 in in diameter were drilled in the spacers for the laser beam to go through.

The electric field plates were mounted to a large aluminum block 8 in from the base of the chamber (see figure 3.2).

The effect of the holes on the electric field was evaluated using a commercial electric field simulation program called Maxwell. The program was unable to analyze the three-dimensional rendering of the plates, so a two-dimensional version consisting of channels instead of holes was done. The results of this showed a reduction of the electric field of 1% in the region with the channels. For the holes, there is less of a gap in the electric field plate than there is with channels, thus there is less of a reduction in the electric field. However, it is unclear how much better this would be. For the measurements discussed here this error is negligible.

3.3.2 Electric Field Switching

The electric fields were switched using two SPDT high-voltage, mechanical relays (Jennings RE6B) rated at 35 kV. A transistor circuit was built to control the 26 V d.c. required to switch. The circuit was designed to receive TTL logic pulses which were generated from a software programmable counter on a data acquisition computer board. This pulse was then sent to a switching circuit which could be set to buffer or invert the TTL signal for each relay independently. In addition, the switching circuit contained a manual override which could position the relays in either position. Thus, the voltage for each electric field plate could be controlled independently. The electric fields were typically switched at a voltage of 10 kV.

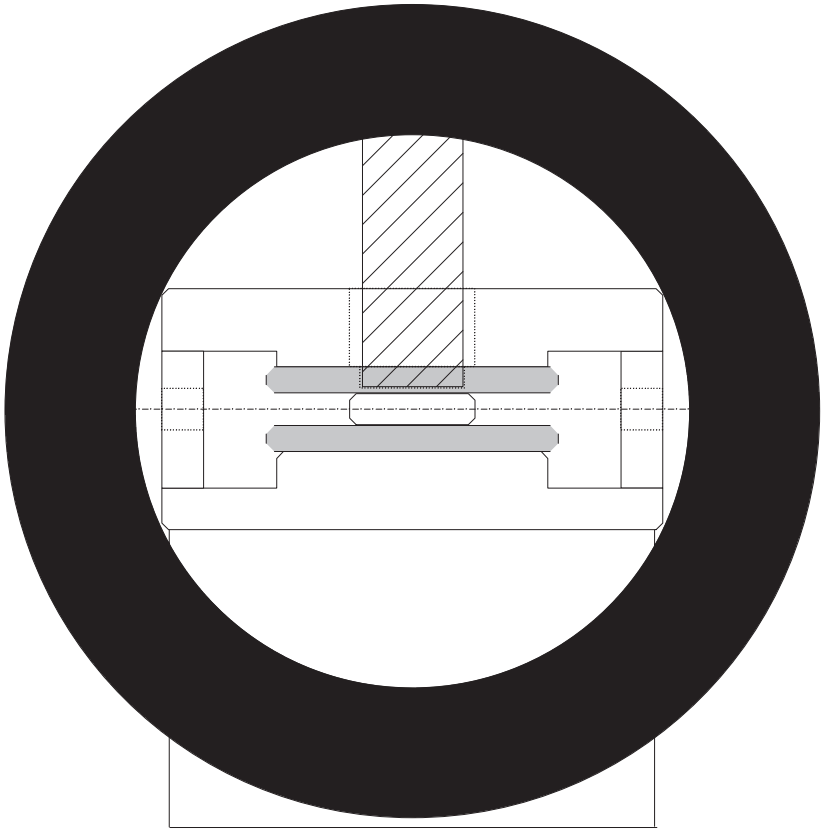

Figure 3.2: Interaction region. Magnetic field coils in black, electric field plates in grey, light guide hatched. Laser beam propagates left to right with polarization out of the page. Atomic beam propagates out of page.

3.4 Magnetic Field Coils

The magnetic field was generated by two coils of 18 AWG copper wire consisting of 1300 turns each. The wire was wrapped on anodized aluminum frames with an inner radius of 3 in. and thickness of 1.4 in. in the radial direction. Epoxy was applied to the wires as they were wrapped in order to create good thermal conductivity and reduce resistive heating of the coils. The coils were mounted to the aluminum block which supported the electric field plates. The separation between the centers of the two coils was 4.25 in.

The configuration was made to approximate a Helmholtz coil configuration, but the large thickness of the coils leads to significant variation from the field generated by Helmholtz coils. The azimuthal and radial fields were calculated over the interaction region using techniques described in reference [18]. The results of this calculation were a magnetic field of

$$B = 94.46\ Gauss\ at\ 0.800\ Amps, \tag{3.1}$$

with a variation of less than 0.1% Gauss over the interaction region. This level of uniformity was sufficient since the asymmetry described in chapter 2 does not depend on the magnitude of the magnetic field, but only on the direction.

The current through each of the coils was controlled by independent bipolar voltage controlled current supplies. Each current supply consists of a monolithic high power op-amps with positive and negative feedback loops. The circuit was designed to give a current of

$$I_{Out} = -0.1 \cdot V_{In}, \tag{3.2}$$

where I_{Out} is the current supplied and V_{In} is the controlling voltage.

3.5 Fluorescence Detection

The transition was detected by measuring the fluorescence in the $6s5d\ ^3P_1 \rightarrow\ 6s^2\ ^1S_0$ decay channel at 556 nm. A ~14in lucite light guide was positioned above the holes in the top electric field plate (see figure 3.2). The light guide was polymerized to a lucite window at the top of the vacuum chamber using dichloroethane. A Burle 8850 photomultiplier tube was positioned on top of the lucite window. In order to reduce background light striking the photomultiplier tube, a 560 nm interference filter with 10 nm full-width-half maximum transmission profile was placed in between the photomultiplier tube and the lucite window.

It was observed that the lucite used for the light guide fluoresced heavily in the 560 nm range when 408 nm light was incident upon it. Consequently, a piece of colored glass with low transmission at 408 nm was epoxied onto the end of the light guide which was closest to the interaction region, thereby reducing the scattered 408 nm light entering the light guide.

The signal from the photomultiplier tube was sent to a current-to-voltage converter which had a low-pass filter with a 1 ms roll-off and a current-to-voltage conversion of

$$V = \left(3 \times 10^6\right) I, \tag{3.3}$$

where I is measured in amps and V in volts. The signal was then digitized by a computer data acquisition board.

Chapter 4

Data and Analysis

The data taken upto this point is very preliminary and its interpretation is consequently limited. The process in which data is taken has not been optimized yet, and there are many areas left to improve before a measurement of the $M1$ amplitude will be possible. Below we discuss how the available data was taken, analyzed, and interpreted.

4.1 Data Acquisition

The data was taken by scanning the frequency of the 408 nm light while switching the electric field. Switching the magnetic field was not done for the data described here, but will be implemented in the future. The laser frequency was scaned with a signal generated by the computer as described in section 3.1. The electric field was switched ~10 times for each frequency point, at a rate of ~0.7 Hz. Data acquisition was triggered with the switching of the electric field. The photomultiplier tube signal, after passing through the current-to-voltage converter, was digitized ~500 times at a rate of ~3000 digitizations per

second beginning immediately after the trigger was received. When the electric field was switched there was a discharge somewhere along the high voltage apparatus. This discharge was probably due to the rearranging of the surface currents on the delrin insulators. It resulted in sparks which were detected by the photomultiplier tube. In order to reduce the effect of these sparks in the data the first 200 digitizations was discarded. The last 300 digitizations were averaged and recorded, giving 1 data point for each electric field state at a given frequency point. In addition, the direction of the electric field was recorded. All of the data was taken on the $M = \pm 1$ magnetic sublevels of isotope ^{174}Yb since it is has the largest isotopic abundance and there is little overlap from the hyperfine components of the odd isotopes (see figure 2.1). The background signal due to scattered light and the dark current of the photomultiplier tube was measured when the frequency of the light was not in resonance with the transition. It was typically around 2 mV, while the signal was ~3 mV. This value was subtracted off from the photomultiplier signal during the analysis. A typical scan is shown in figure 4.1. The scan show good agreement with the results displayed in figure 2.1 with the two $M = \pm 1$ magnetic sublevels of isotope ^{174}Yb splitting and the different magnetic sublevels of ^{173}Yb $F = \frac{5}{2}$ not resolvable.

The scan shows a significant amount of noise, including a large number of outlying points. The source of the noise is not completely understood at this point and will be investigated in the near future. Possible explanations of the outlying points are the frequency doubler losing the lock temporarily, causing the laser power to drop, significantly decreasing the scattered light. If there are still discharges after the first 200 points, they also could increase the noise and may account for the outlying points.

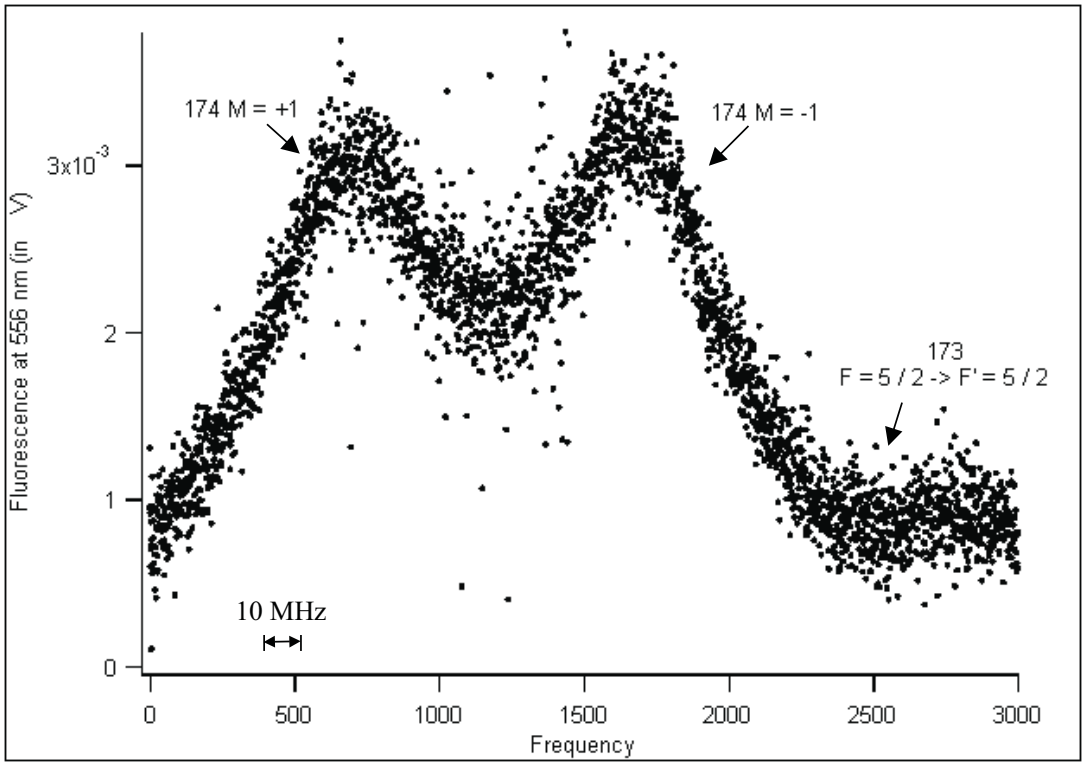

Figure 4.1: Fluorescence in the $^3P_1 \rightarrow {}^1S_0$ decay channel (556 nm) after excitation of the $^1S_0 \rightarrow {}^3D_1$ transition versus the frequency of excitation. Electric field at 10 kV/cm. Magnetic field at 95 Gauss.

4.2 Analysis

The data points were classified according to the frequency of the excitation light and the direction of the electric field, giving ~10 points for every frequency point. For each frequency point, data points corresponding to different directions of the electric field were subtracted. The data points corresponding to the same electric field state were also subtracted. These different combinations were then averaged over each frequency point. Giving the combinations

The distribution of the 300 points averaged for each electric field state was used to calculate the error for each point. The error was used to take a weighted average over each frequency point independent of the direction of the electric field. This data was fit with a two peak fit with each peak consisting of the sum of a Gaussian and Lorentzian. This combination was determined empirically to describe the lineshape for the atomic beam and has no other motivation. The width and amplitudes of the two peaks were held constant since, ignoring the small overlap of isotope 173 $F = \frac{5}{2} \rightarrow F' = \frac{5}{2}$, the two peaks should be of the same height. The effect of the overlap of isotope 173 $F = \frac{5}{2} \rightarrow F' = \frac{5}{2}$ was reduced by considering only those points which were in the upper $\frac{1}{2}$ of the peaks. An example of the fit to the averaged data is shown in figure 4.2.

As the laser frequency scans over the two peaks, the relative amount of the different magnetic sublevels contributing to the signal changes. Thus, the subtracted data with different electric field states should vary as the frequency of the laser varies according to

$$Asymmetry = Signal_+ - Signal_- = \frac{(Peak_{M=+1} - Peak_{M=-1})}{(Peak_{M=+1} + Peak_{M=-1})} \frac{2M1}{\beta E}, \qquad (4.1)$$

where $Signal_+$ is the signal from the photomultiplier tube with a given direction of the

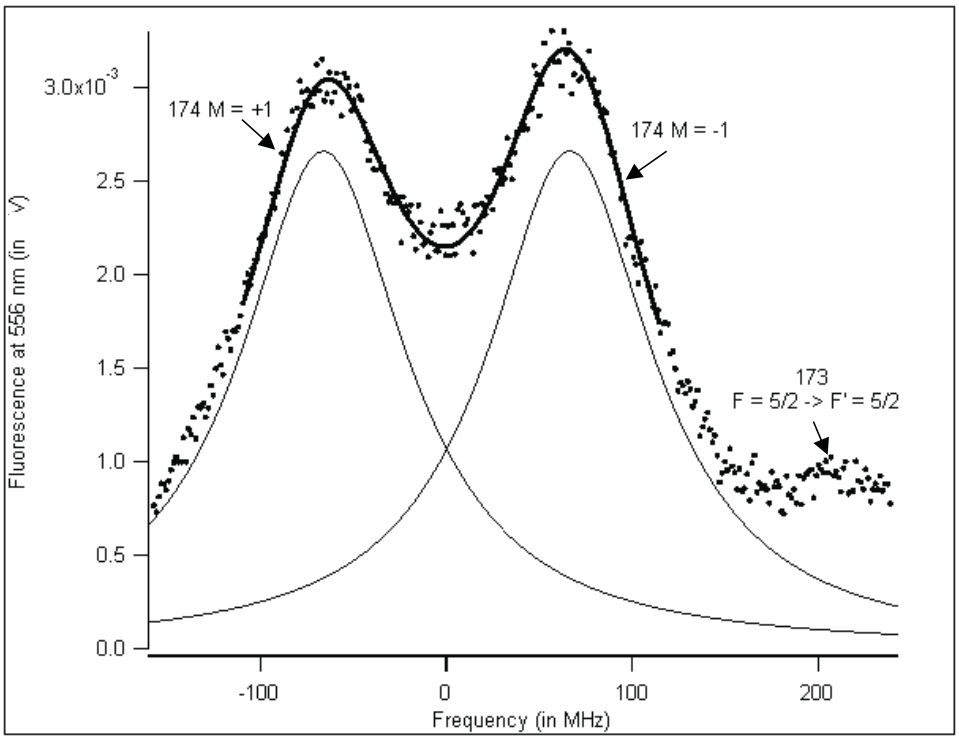

Figure 4.2: Example of fitting of the experimenal averaged fluorescence (thick line) in the $^3P_1 \rightarrow {}^1S_0$ decay channel (556 nm) after excitation of the $^1S_0 \rightarrow {}^3D_1$ transition versus the frequency of excitation. The two individual components (thin lines) are are determined from the fit parameters. Electric field at 10 kV/cm, magnetic field at 95 Gauss.

electric field, $Signal_-$ is the signal with the opposite direction of the electric field, $Peak_{M=+1}$ is the contribution of the $M = +1$ magnetic sublevel to the signal size, and $Peak_{M=-1}$ is the contribution of the $M = -1$ component. The data with the same direction of the electric field should be zero, independent of the frequency of the laser. The values of $Peak_{M=+1}$ and $Peak_{M=-1}$ as a function of frequency were determined from the fit to the averaged signal. In order to account for possible systematic effects which might cause the signal to not be centered around zero, an offset was included to equation 4.1. Thus, the subtracted data was fit as a function of frequency to

$$Asymmetry = \frac{(Peak_{M=+1} - Peak_{M=-1})}{(Peak_{M=+1} + Peak_{M=-1})} A + B, \tag{4.2}$$

where A and B are the fit parameters corresponding to the asymmetry coefficient $\frac{2M1}{\beta E}$ and the offset.

The error for the subtracted data for each frequency point was estimated from the standard deviation of the data points averaged over the frequency point. This estimate of the error was seen to be too small and resulted in a reduced χ^2 much larger than one. This indicates that there is noise at a slow frequency relative to the time of an individual acquisition. The source of this noise has yet to be determined. In order to get a more accurate estimate of the error in the fit parameters, the error on the points was increased until the reduced χ^2 was one. The diagonal elements in the covariant matrix used in the fit were then used to estimate the errors for the fit parameters. For the subtracted data with the same electric field state no asymmetry is expected. This data was analyzed in the same manner to serve as a check on possible systematics.

Run	**Asymmetries for Different Electric Field States**	**Resulting $M1$ Amplitude**	**Asymmetries for Same Electric Field States**
1	0.017(16)	$5.0(48)\times10^{-4}$ μ_B	0.010(16)
2	-0.054(18)	$-1.50(50)\times10^{-3}$ μ_B	0.014(17)
Average	-0.014(12)	-4.6×10^{-4} μ_B	-0.004(11)

Table 4.1: Asymmetries and $M1$ Amplitudes

4.3 Results

The preliminary results described here are from two scans of the laser frequency with an electric field of 10 kV/cm. Interpretation of the data is very limited due to the small amount of data currently available. In addition, there is poor agreement between the two scans. The results of the two scans are presented in table 5.1

The disagreement between the two scans suggests that there may be systematic effects which are varying with time. Although what these effects may be remains to be determined. Thus, using the error on the individual scans to estimate the error for the combined value is not realistic. The error quoted above was determined from the variation of the results of the two scans. Since only two scans are currently available the uncertainty in the error is relatively large. However, we place a preliminary upper limit on the $M1$ amplitude of

$$|M1| < 3 \times 10^{-3}\ \mu_B, \tag{4.3}$$

with a confidence level of ~95%.

4.4 Systematic Errors

At present, any systematic errors due to misalignments of the various fields are much smaller than the error associated with the statistics from the data currently available. However, the issue of systematic effects will become important when the noise is decreased. The effects of misalignments was studied by performing an analysis similar to that described in section 2.4 using arbitrarily directed fields. The direction of the magnetic field was used to define the z-axis and the direction of propagation, the direction of the electric field, and the polarization were allowed to deviate from their nominal values. In addition, the polarization was allowed to be elliptical, with the phase chosen to make the z-component real. The results of the calculation reveal that using the analysis described above, the $M1$ amplitude measurement is relatively insensitive to misalignments. Any misalignment must coincide with a second, or even third, misalignment if an effect is to be observed in the value of the $M1$ amplitude. If, for example, the direction of propagation of the light were misaligned by ~10° towards the y-axis and the electric field were misaligned by ~10° towards the x-axis, the value of the $M1$ amplitude measured would be off by less than 1%. In addition, there is no misalignment which can lead to an asymmetry which is not proportional to the $M1$ amplitude.

The second source of systematic errors to consider is imperfect switching of the electric fields. Here too, the method of measurement is relatively insensitive to error. Because the asymmetry relies on the changing sign of the $M1$ interference term as the laser frequency scans over the magnetic sublevels, an error in the switching of the electric field leads will not effect the value of the asymmetry coefficient, but will only lead to a constant

offset of the asymmetry signal.

With the robust nature of the experiment it might appear that the switching of the magnetic field is not necessary. However, switching of the magnetic field allows for a higher frequency lock-in detection which will eliminate the low frequency noise present in the data taken so far. In addition, switching of the magnetic field also leads to an asymmetry which is insensitive to imperfections in the switching. The $M1$ amplitude does not depend on the magnitude of the electric field (see equation 2.32). Consequently, the magnetic field only has to be switched well enough that the Zeeman shift is not significantly different for the two magnetic sublevels.

Chapter 5

Conclusion

The measurement of the $M1$ amplitude is far from complete. However, the above data provides a guide as to what improvements must be made in the near future. The most immediate step is to improve in the short-term noise of the fluorescence detection. With the current noise it will not be possible to measure down to the 10^{-4} μ_B in a realistic period of time. At present, the source of the noise is unknown, but is far above the theoretical, shot noise limit. It is also necessary to find a solution to the problem of the water vapor in the doubling cavity so that the new LBO crystal can be used, allowing for significantly more power, thereby improving the signal size. Once these improvements are made we will be able to better assess systematic effects which might lead to false asymmetries. This will entail switching the magnetic field, as well as the electric field, to provide an additional check on the value measurement. Although many improvements are necessary before we achieve the sensitivity necessary to make a measurement of the $M1$ amplitude, there do not appear to be any major setbacks.

Bibliography

[1] C. Cohen-Tannoudji, B. Diu, and F. Laloë. *Quantum Mechanics*. John Wiley and Sons, New York, New York, 1977.

[2] M.A. Bouchiat and C.C. Bouchiat. Phys. Lett. 48B:111, 1974.

[3] M.A. Bouchiat and C.C. Bouchiat. Rep. Prog. Phys. 60:1351, 1997.

[4] P.A. Vetter et.al. Phys. Rev. Lett. 74:2658, 1995.

[5] C.S. Wood et.al. Science. 275:1759, 1997.

[6] D. DeMille. Phys. Rev. A. 74:4165, 1995.

[7] V.A. Dzuba, V.V. Flambaum, and I.B. Khriplovich. Zeitschrift fur Physik D. 1:243, 1986.

[8] S.G. Porsev, Yu.G. Rakhlina, and M.G. Kozlov. Pis'ma Zh. Eksp. Teor. Fiz. 61:449, 1995.

[9] C.J. Bowers et al. Phys. Rev. A. 53:3103, 1996.

[10] C. J. Bowers. PhD thesis, Berkeley, California, 1998.

[11] A. Corney. *Atomic and Laser Spectroscopy.* Clarendon Press, Oxford, England, 1977.

[12] J.R.P. Angel and P.G.H. Sandars. Proc. Roy. Soc. 305:125, 1968.

[13] W.C. Martin, R. Zalubas, and L. Hagan. *Atomic Energy Levels: The Rare Earth Elements. NBS.* U.S. Government Printing Office, Washington D.C., 1978.

[14] I. I. Sobelman. *Atomic Spectra and Radiative Transitions.* Springer Verlag, New York, New York, 1979.

[15] R.D. Cowan. *Theory of Atomic Structure and Spectra.* University of California Press, Berkeley, California, 1981.

[16] R.W.P Drever et al. Appl. Phys. B.

[17] T.W. Hansch and B. Couillaud. Optics Communication. 35:441, 1980.

[18] R.C. Calhoun. Amer. Jour. of Phys. 64:1399, 1996.